Characterizing and Commissioning the Sutherland High-Speed Optical Cameras (SHOC)

R. Coppejans,[1,2,3] A. A. S. Gulbis,[1,4,5] M. M. Kotze,[1] D. L. Coppejans,[2,3] H. L. Worters,[1] P. A. Woudt,[2] H. Whittal,[1] J. Cloete,[1] AND P. Fourie[1]

ABSTRACT. Two identical new instruments, the Sutherland High-speed Optical Cameras (SHOC), have been developed for use on the South African Astronomical Observatory's (SAAO) 1.9, 1.0 and 0.75 m telescopes at Sutherland. The SHOC systems are fast-frame-rate, accurately-timed, high-quality, visible-wavelength imagers. Each system consists of a camera, global positioning system (GPS), control computer and peripherals. The primary component is an Andor iXon X3 888 UVB camera, utilizing a 1024×1024 pixel, frame-transfer, thermoelectrically-cooled, back-illuminated CCD. One of SHOC's most important features is that it can achieve frame rates of between 1 and 20 frames/s during normal operation (dependent on binning and subframing) with microsecond timing accuracy on each frame (achieved using frame-by-frame GPS triggering). Frame rates can be increased further, and fainter targets observed, by making use of SHOC's electron-multiplying (EM) modes. SHOC is therefore ideally suited to time domain astronomy where high frame rates and extremely accurate timing are critical. Here, we present details of the instrument components, characteristics measured during commissioning, science demonstrations, and development plans. Attention is specifically given to exploration of the signal-to-noise (S/N) parameter space as a function of EM and conventional modes. These results enable observers to optimize instrumental settings for their observations and clearly demonstrate the advantages and potential pitfalls of the EM modes.

1. INTRODUCTION

Researchers in South Africa have carved out a niche in the field of high-time-resolution astronomy, with programs including stellar occultations by minor planets (e.g., Gulbis et al. 2006; Elliot et al. 2010), extrasolar planetary transits (e.g., Pepper et al. 2012), accretion in cataclysmic variable star systems (e.g., Buckley et al. 2010; Woudt et al. 2010), properties of eclipsing polar binaries (e.g. O'Donoghue et al. 2006; Potter et al. 2011), and accretion-induced optical flickering in recurrent novae (e.g., Worters et al. 2007). The Sutherland High-speed Optical Cameras (SHOC 1 and SHOC 2) are two new instruments that cater to high-time-resolution imaging and can be mounted on the 1.9, 1.0 and 0.75 m telescopes at the South African Astronomical Observatory's (SAAO) Sutherland site.

High-speed photometry combined with microsecond timing accuracy and minimal dead time are features that were not available on these telescopes prior to SHOC. In addition, SHOC's high quantum efficiency across the visible wavelength range, low dark current and low read noise ensure excellent data quality for all imaging projects. One unique capability of SHOC is the option to employ electron-multiplying (EM) technology (initially described by Hynecek 2001; Jerram et al. 2001). In EM mode, electrons are transferred through an extended serial register in which they undergo impact ionization, strengthening the observed signal before read noise is added in the output. This effectively reduces read noise to subelectron levels, allowing a significant increase in data quality for photon-starved applications. Finally, SHOC also features a range of user selectable parameters such as custom binning and subframing, two or three electron to analog-to-digital unit (ADU) gain settings and four readout amplifiers (two for conventional operation and four for EM). These features allow users to optimize their observations, thereby increasing data quality and exceeding previous instrumental and magnitude limitations.

Details of the instruments and the telescopes on which they can be mounted are presented in § 2. Data quality is addressed in § 3, where equations for predicted signal-to-noise ratios (S/Ns) are derived as a function of the mode of operation (conventional vs. EM), target magnitude and exposure time. Section 4 contains a selection of science demonstrations to exemplify SHOC's capabilities.

[1] South African Astronomical Observatory, P.O. Box 9, Observatory, 7935, South Africa; rocco.coppejans@gmail.com.

[2] Astrophysics, Cosmology and Gravity Centre, Department of Astronomy, University of Cape Town, Private Bag X3, Rondebosch 7701, South Africa.

[3] Department of Astrophysics/Research Institute for Mathematics, Astrophysics and Particle Physics, Radboud University Nijmegen, P.O. Box 9010, 6500 GL Nijmegen, Netherlands.

[4] Southern African Large Telescope, P.O. Box 9, Observatory 7935, Cape Town, South Africa.

[5] Department of Earth, Atmospheric, and Planetary Sciences, Massachusetts Institute of Technology, Cambridge, MA 02139.

976

While this article presents the instruments to the general astronomical community, a detailed description of all components and commissioning tests can be found in Coppejans (2013).

2. INSTRUMENT SPECIFICATIONS

SHOC's design is based on two existing instruments, the Portable Occultation, Eclipse and Transit Systems (POETS; Souza et al. 2006) and the Massachusetts Institute of Technology Optical Rapid Imaging System (MORIS; Gulbis et al. 2011). SHOC most notably differs from these instruments in the mounting mechanism and a larger format CCD. Each SHOC system consists of an Andor iXon X3 888 UVB camera, a Spectrum Instruments Inc. Intelligent Reference/TM-4™ global positioning system (GPS), a control computer, and connecting power supplies and cables. The primary components are described in detail below. The GPS, computer and camera power supply are housed in a custom-built aluminum control crate operating on a single power switch and requiring only a few cable connections for functionality. Three complete control crates were built; however, there are only two cameras. This configuration allows SHOC systems to be mounted on two different telescopes simultaneously, with the third control crate serving as a backup in the case of hardware failure. A summary of instrument characteristics is provided in Table 1.

2.1. Telescopes and Mounting

SHOC can be mounted on the SAAO's 1.9, 1.0 and 0.75 m telescopes in Sutherland. The telescopes are located within 200 m of one another—for reference, the 1.0 m is at latitude S32°22.78′, longitude E20°48.60′ and altitude 1810 m. All three of these telescopes are polar mounts with approximate focal ratios of f/18, f/16 and f/15, respectively. Each of the telescopes has a filter box that can hold either two (in the case of the 1.9 m and 1.0 m) or one (0.75 m) filter wheel. Available filters include Bessel $UBVRI$, Sloan $u'g'r'i'z'$ and Stromgren $uvby$ filters.

Figure 1 is a schematic of the instrument setup. The camera is mounted at the Cassegrain focus directly below the filter wheel box via a mounting plate. The control crate is bolted to the bottom of the telescope. SHOC was designed to have small, lightweight components; therefore, it has minimal impact on telescope balance. The camera connects to the control crate via three cables (one each for camera control, GPS triggering and

TABLE 1
SUMMARY OF INSTRUMENT CHARACTERISTICS

Characteristic	Value
Serial number	SHOC 1: X-5982; SHOC 2: X-6448
CCD	E2V CCD201; 1024×1024, 13 μm^2 pixels
Quantum efficiency	35% for $\lambda < 375$ nm; >90% for $\lambda \sim 480–700$ nm; <40% for $\lambda > 900$ nm
Full well capacity[a]	143838 e^- for SHOC 1; 79169 e^- for SHOC 2
Linearity[a]	<1%
Readout rate[b]	0.9 frames s^{-1} (full frame, 1 MHz CON amplifier);
	7.9 frames s^{-1} (full frame, 10 MHz EM amplifier);
	9.0 frames s^{-1} (full frame, binned 4×4, 3 MHz CON amplifier);
	$\sim$100 frames s^{-1} with binning and subframing
Dead time	6.7 ms (for 1024 rows at the default vertical shift speed)
Read noise[c]	5.8 to 15.8 e^- pixel^{-1} and 18.0 to 83.3 e^- pixel^{-1} (SHOC 1; CON and EM)
	6.0 to 14.0 e^- pixel^{-1} and 16.5 to 69.6 e^- pixel^{-1} (SHOC 2; CON and EM)
Gain[c]	0.6 to 11.0 e^- ADU^{-1} and 3.6 to 52.4 e^- ADU^{-1} (SHOC 1; CON and EM)
	0.7 to 9.9 e^- ADU^{-1} and 3.4 to 44.9 e^- ADU^{-1} (SHOC 2; CON and EM)
Dark current[d]	<0.001 e^- pixel^{-1} s^{-1}
Single frame timing accuracy	<10 μs using frame-by-frame GPS triggering
	$\sim$1 s using the computer clock
GPS antenna cable delay	75.8 ns (1.9 m telescope); 30.3 ns (1.0 m telescope);
	20.2 ns (0.75 m telescope)[e]
GPS trigger cable delay	15.2 ns[e]

[a]Dependent on the camera. The saturation signal per pixel and linearity up to saturation (as a percentage variation from a straight-line fit) are provided by the manufacturer and confirmed with laboratory tests. Linearity measurements for three different camera modes for SHOC 1 are provided in Figure 3.

[b] Dependent on the readout amplifier, binning, and subframing. Examples are provided for reference.

[c]Read noise and gain are discrete values within these ranges, based on the selected amplifier (1 or 3 MHz for CON and 1, 3, 5, or 10 MHz for EM) and gain setting (approximately $1\times$, $2.5\times$, or $5\times$ for all amplifiers except 10 MHz, which has only $2.5\times$ or $5\times$). Values are provided in the manufacturer specification sheets and were confirmed by laboratory tests.

[d]Dark current was found to be negligible in exposures up to 1200 s at $< = -40°C$ in both cameras. This is consistent with the manufacturer's specification.

[e]Based on a manufacturer-specified time delay of 5.05 ns m^{-1} for 15 m (1.9 m telescope), 6 m (1.0 m telescope) and 4 m (0.75 m telescope) of RG-58 antenna cable and for 3 m of RG-174 trigger cable (all telescopes).
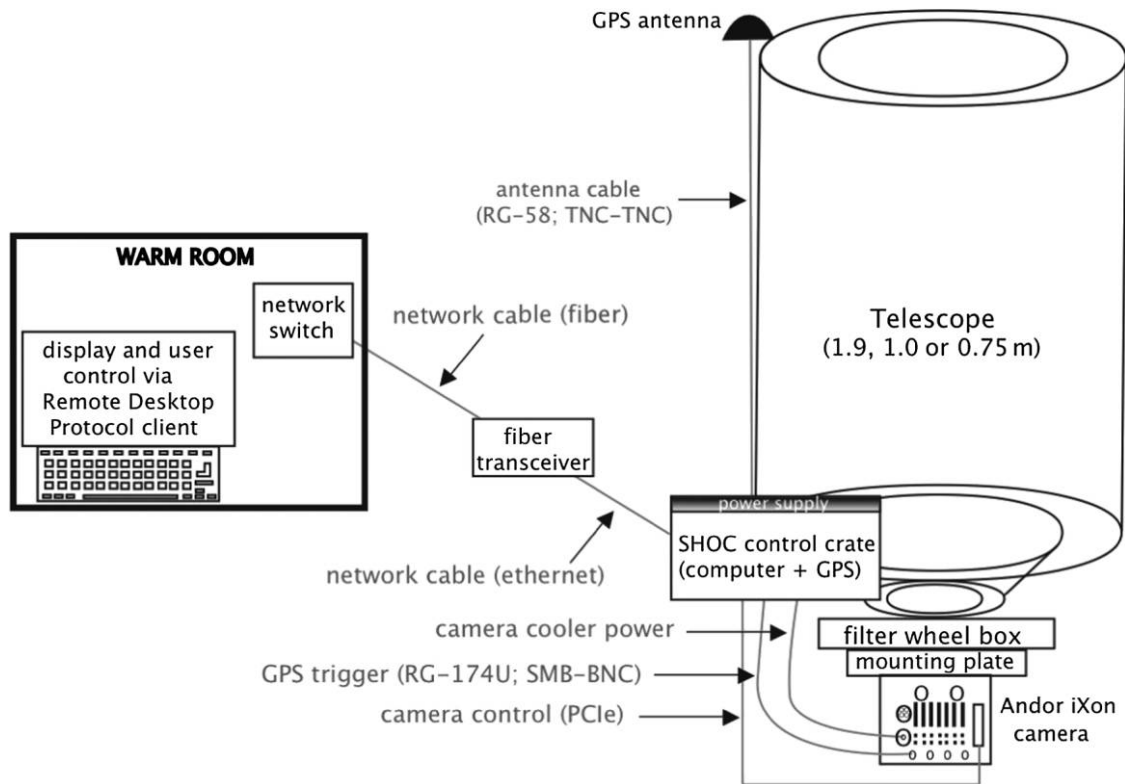
FIG. 1.—Schematic illustrating SHOC's mounting and setup, with cables shown in gray. The 1.9 m telescope can have a focal reducer mounted between the filter wheel box and the mounting plate. The drawing is not to scale.

cooling power). In turn, the control crate is connected to a power outlet and an ethernet port on the telescope. The GPS is also connected to an all-weather antenna mounted at the end of the telescope tube. Connecting the control computer to the SAAO intranet allows SHOC to be operated from the warm room. This will also allow SHOC to be used during remote observing should one of the telescopes be modified in the future to allow remote operation. Note that a focal reducer can be mounted on the 1.9 m, increasing the field of view (FoV) at the cost of throughput.

2.2. Cameras

Each SHOC camera utilizes a frame-transfer, thermoelectrically-cooled, back-illuminated CCD with 1024×1024 pixel imaging area. The peak quantum efficiency (QE) is $>95\%$ at $\lambda \sim 550$ nm, dropping off to $\sim 60\%$ at 400 nm and 850 nm. At shorter wavelengths ($\lambda < 375$ nm) a UVB coating maintains the QE at 35%. The QE curve for the camera is provided in Coppejans (2013) and on the Andor iXon X3 specification sheet. The cameras employ efficient thermoelectric coolers that reach and maintain a typical operating temperature of $-60°$C within a few minutes of start up. Additional cooling down to $-100°$C is possible using a water flow. Since no dark current could be detected in 20 minute exposures when operating at

temperatures between $-40°$C and $-70°$C in the laboratory, water cooling is not used.

A subframe of the CCD can be selected, either of a standard half- or quarter-sized frame or of a user-defined size and location. The readout time can be slightly decreased as a function of subframing—depending on the location and size (e.g., subframes at the bottom of the CCD containing a smaller number of rows will read out the fastest). The CCD can also be binned to user-specified values where the vertical and horizontal binning do not need to be the same. In the case that the imaging area is not evenly divisible by the desired binning, the software will automatically create a subframe to allow the maximum number of superpixels within the selected area. Binning occurs after the CCD is read out into the shift register; therefore, it will decrease the overall readout time but will not affect the dead time.

The Andor iXon camera allows readout via a conventional (CON) or electron- multiplying (EM) output amplifier with horizontal pixel shift speed of 1 or 3 MHz in the CON mode and 1, 3, 5 or 10 MHz in the EM mode. In both the EM and CON modes, the 1 MHz amplifiers employ a 16 bit analog-to-digital converter (ADC) while the 3, 5, and 10 MHz amplifiers utilize a 14 bit ADC. The read noise varies as a function of readout amplifier, with the ranges of values listed in Table 1. The 1 MHz CON mode offers a remarkably low read noise of approximately $6 \ e^{-} \ \text{pixel}^{-1}$ while the 3 MHz CON mode allows higher frame

rates at the expense of slightly higher read noise (minimum of roughly 10 e^- pixel^{-1}). Electrons going through the EM registers are multiplied by the EM gain, a parameter that can be set to a value between 1 and 1000. This process effectively decreases the read noise by a factor of 1 over the EM gain. Laboratory tests were conducted in which the EM gain was stepwise increased from 1 to 300, and the effective read noise was calculated at each EM gain using Janesick's method (Janesick 2001). These tests confirmed that effective read noise drops below 1 e^- pixel^{-1} when an EM gain value just above the specified read noise (as defined when EM gain = 1) is used in all of the EM modes of both SHOC cameras. An example of measured and predicted effective read noise as functions of EM gain is shown in Figure 2.

Note that the low-read-noise benefit of the EM modes comes at a cost: EM reduces the dynamic range, incurs an excess noise factor and increases clock-induced charge (CIC). First, the dynamic range is inherently higher for CON modes because the EM register has the same full-well depth but higher read noise. As a function of EM gain, the dynamic range increases at lower EM gains as read noise is effectively reduced. Once the register can no longer accommodate the amplified signal, the dynamic range levels out. When the effective read noise falls below single-photon levels, the dynamic range drops with increasing EM gain. Second, the excess noise factor is the result of the stochastic nature of the EM process and, at large gain, is equal to the square root of two (e.g., Basden & Haniff 2004). Finally, clock-induced charge is electrons that are generated during the CCD readout. These signals are amplified by the EM register
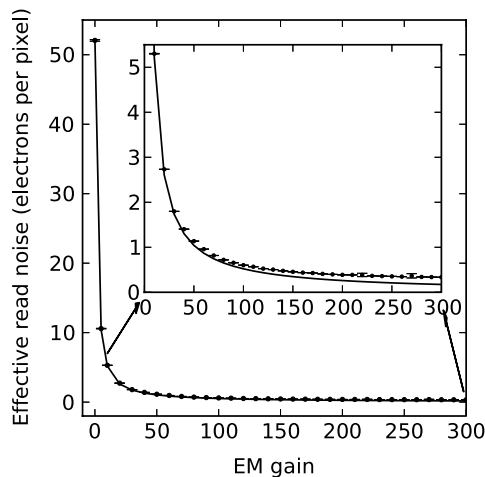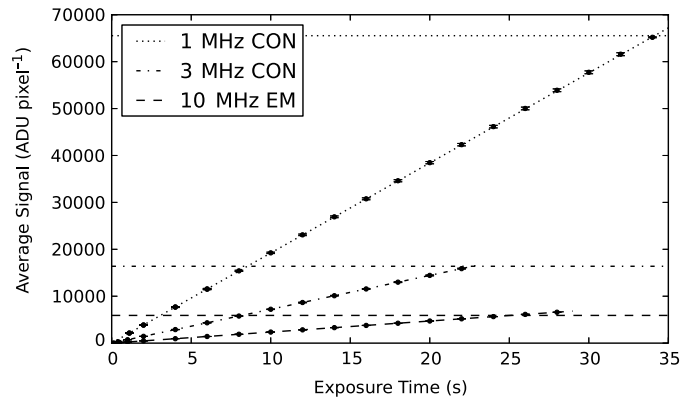

FIG. 3.—Linearity measurements for SHOC 1, with 2.4× gain. Average ADUs per pixel are plotted as points (with error bars too small to be apparent) along with the best-fit lines. Saturation limits, in this case each due to the 16 or 14 bit electronics, are indicated by *horizontal lines* with the same style as the corresponding best-fit line. The percentage deviation between the data and the lines has an average of 0.2%. The measurements for SHOC 2 are similar.

and become an increasingly significant factor with increasing EM gain (e.g., Daigle et al. 2009).

To determine the linearity for each of the modes, tests were conducted to measure ADUs as a function of increasing exposure time. All of the modes for SHOC 1, and the 1 and 3 MHz CON and EM modes for SHOC 2, were found to be linear to within 0.5% for counts between the bias level and saturation. The 5 and 10 MHz EM modes on SHOC 2 were found to be linear to within 1.5% and 3.0% over the same count range. For demonstration, a subset of the linearity measurements is plotted in Figure 3.

In order to measure the CCD plate scale and derive values for the FoV on each telescope, the open cluster NGC 2243 was observed using 1×1 binning. The angular separations between six or more pairs of stars were obtained from the WEBDA database (http://www.univie.ac.at/webda/) while the pixel separations between the stars were found using IRAF's (Tody 1986) IMEXAMINE task, which outputs a centroid value calculated using a marginal distribution method. The angular separations are divided by the pixel separations to obtain values for the plate scale. The mean and standard deviation from the measured pairs of stars return the final values for plate scale and FoV presented in Table 2.

FIG. 2.—Effective read noise plotted as a function of EM gain for SHOC 2 in the 10 MHz EM mode, which has specified read noise of 52 e^- pixel^{-1}. Measured values are plotted as points (with error bars too small to be discernible) while theoretical values (read noise divided by EM gain) are shown as a solid line. The insert shows the bottom section of the graph magnified, illustrating that the effective read noise drops below 1 e^- pixel^{-1} at an EM gain just above 50.

2.3. Timing

The Spectrum Instruments, Inc. Intelligent Reference/ TM-4™ GPS provides absolute timing accuracy, having manufacturer specification of ±25 ns from UTC with root-mean-square stability of 12.5 ns. Notably, the GPS allows a programmable output pulse. The programmable output can be set to one pulse of fixed width, or as a series of perpetual, fixed-width pulses at a specified interval. Antennas are permanently mounted

Telescope	Plate scale (arcsec/pixel)	Field of view (arcmin/side)
1.9 m without focal reducer	0.076 ± 0.001	1.29 ± 0.01
1.9 m with focal reducer	0.163 ± 0.001	2.79 ± 0.01
1.0 m	0.167 ± 0.001	2.85 ± 0.01
0.75 m	0.218 ± 0.001	3.73 ± 0.01

on top of each of the telescope tubes and connect to the GPS via an RG-58 coaxial cable. While four satellites are required in order for accurate values of latitude, longitude, altitude and time to be determined, only a single satellite is required for an accurate time if the location is known and fixed. The GPSs were used to determine locations of each telescope, and those locations are entered when the GPS is initialized. The GPS antennas are mounted inside of the domes, which does result in the GPS being shielded from satellites while the domes are closed. However, sufficient signal from at least three satellites was obtained during observations from all telescopes while the domes were open.

The iXon cameras accept an input trigger from the GPS via an RG-174 coaxial cable of known length and thus known timing delay. The cameras can operate in two modes with respect to image timing. From the least to the most accurate, the modes are as follows: (i) "internal trigger," where the Andor camera software is used to take a series of exposures that are time stamped from the control computer (accuracy ~1 s) and (ii) the readout of each exposure can be triggered by a separate GPS pulse (accuracy of all frames to better than ~10 μs).

2.4. Control Computers

There were several design specifications for the SHOC control computers. The first was a preference for small form, to allow easier mounting on the bases of the telescopes. A PCIe or PCI-X slot was required to allow interfacing with the cameras, and a serial port was required to allow interfacing with the GPS (although a serial to USB adapter could be used). In addition, the hard drive speed was required to be at least 10,000 revolutions per minute (rpm) to allow fast data acquisition.

We were unable to source an off-the-shelf computer matching all of the requirements, thus we ordered components and custom built each control computer. The components are a Silverstone SUGO SG05B Mini-ITX chassis (~7 in. × 9 in.× 11 in.), an Intel DH7KG Jet Geyser LGA 1156 motherboard (with PCIe slot and serial port), an Intel Dual Core i3-540 3.06 GHz CPU, a 300 GB 10,000 rpm Western Digital VelociRaptor hard drive and 4 GB of RAM. The operating system was chosen to be 32 bit Windows XP, which allows compatibility with the Spectrum Instruments, Inc. GPS software and the Andor Solis (Solutions for Imaging and Spectroscopy) software. The computers are connected to the local intranet via an ethernet cable to a fiber transceiver. Fibers and transceivers

are permanently mounted on each telescope and in each control room, where the fibers connect to a network switch. Any computer on the local network can connect to the SHOC computers using a remote desktop protocol: the SAAO Linux client provided to observers at the telescopes connects to SHOC via rdesktop (open source software provided under GNU public license).

Currently, SHOC employs the manufacturer's software to operate the primary components. Thus, the information from the camera, GPS and telescope is independent. Data are stored in multiextension FITS (Flexible Image Transport System) format. Each file, or data cube, is composed of a user-selectable number of single frames with a single header. FITS headers include only the camera parameters, requiring users to separately record telescope information (such as pointing, airmass, filters, etc.), GPS timing information (if used) and target information.

3. SIGNAL-TO-NOISE RATIOS IN DIFFERENT MODES

Of critical importance to SHOC users is the optimization of the camera parameters to obtain the highest possible data quality. While the S/N that can be obtained on a target provides a measurement of data quality, the most definitive camera parameter that will influence the S/N is whether the CON or EM register is used. In order to predict S/N values, sets of standard stars were selected from Landolt (1992) and observed in EM and CON modes on each of the telescopes. The observations were taken on photometric nights, with each target observed over two data cubes, containing three consecutive frames, separated by approximately a minute. The Bessel V filter was employed, using an exposure time such that the stars were photon-noise limited. The stars were observed over the largest possible range of air masses (typically between 1 and 2.3) and ranged in magnitude between 9 and 13.

In order to derive instrumental magnitudes, the frames were first bias subtracted and flat-fielded (using master biases and flats) before using IRAF's PHOT task (Stetson 1987) to extract the magnitude, magnitude error and total number of ADU of the star. An aperture radius of 3 times the full width at half-maximum (FWHM) was selected, using the largest FWHM for all of the frames in the cube. This aperture size was chosen because it contains 98% of the total stellar signal (Merline & Howell 1995). Next, the magnitude error and sky-subtracted stellar signal values for the frames in each cube were combined into a single value by means of averaging and error propagation (this could be done as the change of air mass throughout each cube was negligibly small). Since it is typically not possible to correct for atmospheric variations when doing aperture photometry, and methods such as the one described by Honeycutt (1992) cannot be applied due to small number statistics, the error values were artificially increased such that the uncertainties of points at equal air mass overlap.

For each telescope, extinction coefficients and zero-point magnitudes were derived by fitting a line to the difference between the instrumental and catalog magnitudes (obtained from Landolt 1992) as a function of air mass. The photoelectron flux for each standard star was obtained by applying the derived values to the total signal inside of the aperture in order to correct for air mass and instrumental offset, multiplying by the appropriate gain and dividing by the exposure time. By fitting a straight line to standard star fluxes as a function of their magnitudes, values for the expected flux (inside an aperture of 3 times the FWHM) can be estimated for a star with arbitrary magnitude. Note that photometric and fitting errors are propagated at all steps and appropriately incorporated into the final error values.

3.1. Calculating Predicted S/Ns

The predicted S/N values were calculated using the following equations:

$$(S/N)_{CON} = \frac{Sn_{pix}t}{\sqrt{n_{pix}t(S + S_{sky}) + n_{pix}\sigma_R^2}} \quad (1)$$

and

$$(S/N)_{EM} = \frac{Sn_{pix}t}{\sqrt{F^2 n_{pix}t(S + S_{sky}) + n_{pix}\sigma_R^2 g^{-2}}}, \quad (2)$$

where S is the flux in photons per pixel per second for the target, S_{sky} is the flux in photons per pixel per second from the sky background, t is the exposure time in seconds, n_{pix} is the number of pixels in the aperture, σ_R is the read noise in electrons per pixel, F is the excess noise factor (assumed to be equal to the square root of two, as noted in § 2.2) and g is the EM gain. Dark current is ignored in these calculations, as lab tests showed that it is negligible in exposures up to 20 minutes. Furthermore, the contribution from CIC was ignored in equation (2), as Gach et al. (2009) found that CIC only becomes significant at flux levels below 1 photoelectron/pixel/s, which is lower than the expected flux levels for most SAAO observers.

To predict the S/N of an observation, the value for S is estimated as the expected flux for that magnitude, derived from standard star observations in § 3.1. The flux S_{sky} is found by assuming a sky surface brightness (values of 21.7 mag arcsec^{-2} and 19.7 mag arcsec^{-2} were used for dark and bright conditions, respectively), which is converted to a sky magnitude inside the aperture and then to a flux as derived in the previous section.[6,7]

---

[6]The average dark sky background measured at Sutherland between 1986 and 2012 (R. Sefako, 2012, private communication).

[7]The value 19.7 mag arcsec^{-2} was chosen as Krisciunas & Schaefer (1991) found that under a three quarters moon, the sky brightness in the V band increases by about 2 mag at a position angle of 90° from the moon.

In order to test the predicted S/N values, a set of four different Landolt (1992) standard stars of magnitude $V = 12.22$, 13.01, 14.34 and 15.02 were observed in the V filter with exposure times between 1 and 30 s on the 1.0 m using SHOC 2 in the 1 MHz 2.5× CON mode. This test was assumed to be representative of both cameras. For each star at each exposure time, 20 single frames were taken. Aperture photometry was performed using IRAF's PHOT task, allowing the S/N to be determined from the output signal inside an aperture of 3 times the FWHM. The mean and standard deviation of the S/Ns were calculated for each exposure time. The average difference between the measured and predicted S/N values was found to be less than 4% for each star.

In a similar test, Figure 4 compares the S/Ns that can be obtained in the EM and CON modes. Here, a $V = 15.6$ star was observed on the 1.9 m without the focal reducer, using SHOC 1 in the 1 MHz 2.4× CON and EM modes, at a range of exposure times between the minimum (0.15 s cycle time) and 13 s with EM gain of 1, 20 and 60. In this case, the average deviation between the measured and predicted S/Ns was found to be at maximum 13% for each mode.

The reason for the difference between the measured and predicted S/Ns is that the data used to test the values were taken on different nights. Accordingly, it is expected that the value would differ due to differences in atmospheric (primarily extinction coefficients, lunar illumination and cloud cover) and telescope conditions. Nonetheless, these tests serve to show that although the predicted S/N values will not give the exact S/N that will be
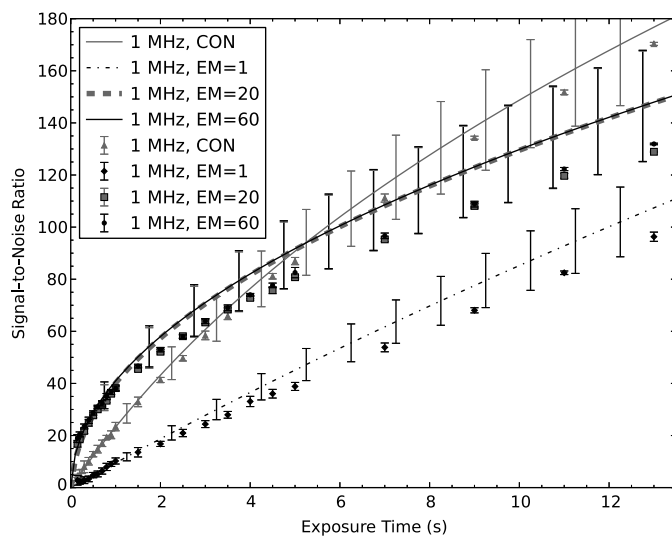

FIG. 4.—Comparison of measured (*points*) and predicted (*lines*) S/Ns of a $V = 15.6$ mag star star observed on the 1.9 m without the focal reducer, using SHOC 1 in the 1 MHz 2.4× CON and EM modes. Error bars are plotted on both measured and predicted values and were found to differ by a maximum of 13% for each mode. The predicted values for the EM = 20 and EM = 60 modes appear to lie on top of each other at this scale, differing by an average of 0.75 S/N units over the range of exposure times.

obtained on a specific night, they do provide a reasonable estimate. Note, for the purpose of these tests, that the effect of sky brightness on the S/N was ignored.

The data of the $V = 15.6$ star clearly demonstrate that higher S/N will be obtained in the EM modes (compared to the CON modes) as long as the read noise term is dominant over the photon noise term in equation (2). Figure 4 also shows an increase in S/N as a function of increasing EM gain only to the point where read noise dropped below $1\ e^-\ \mathrm{pixel}^{-1}$. This effect is to be expected when considering equation (2). Increasing the EM gain beyond this value only serves to decrease the dynamic range without significantly increasing the S/N. In this case, the effective read noise was expected to drop below $1\ e^-\ \mathrm{pixel}^{-1}$ at an EM gain slightly above 20. In fact, increasing the EM gain from 20 to 60 only increased the S/N by an average value of 0.75 S/N units over the entire range of exposure times.

3.2. EM Versus CON and Observing Strategy

To determine which mode should be used to return the highest quality data, the exposure time at which the S/Ns are equal is considered. Setting equations (1) and (2) equal to each other returns the exposure time for equal S/Ns in EM and CON modes:

$$t_{\mathrm{EM=CON}} = \frac{1}{(S + S_{\mathrm{sky}})}\left(\sigma_{\mathrm{CON}}^2 - \frac{\sigma_{\mathrm{EM}}^2}{g^2}\right), \qquad (3)$$

where σ_{CON} and σ_{EM} are the read noise in electrons per pixel in the CON and EM modes, respectively.

Equation (3) is graphically illustrated in Figure 5, where the exposure time at which S/Ns are equal in EM and CON modes is plotted as a function of stellar magnitude and sky surface brightness for both cameras in the 1 and 3 MHz modes. For each magnitude, using an exposure time larger than the plotted value will result in a higher S/N in the CON mode, while an exposure time less than the value will result in a higher S/N in the EM mode.

In order to guide observers in selecting the best mode, exposure time and lunar conditions to observe their target, the equations for the predicted S/N (derived in the previous section) are provided in the SHOC user manual.[8] From these equations, plots such as that shown in Figure 6 can be generated allowing an observer to make an educated decision and obtain the best data for their specific need. In addition, when submitting an application, observers should keep in mind that there is more competition for time on the larger telescopes. Observers are therefore advised to apply for the smallest telescope on which the desired S/N and time resolution can be obtained.

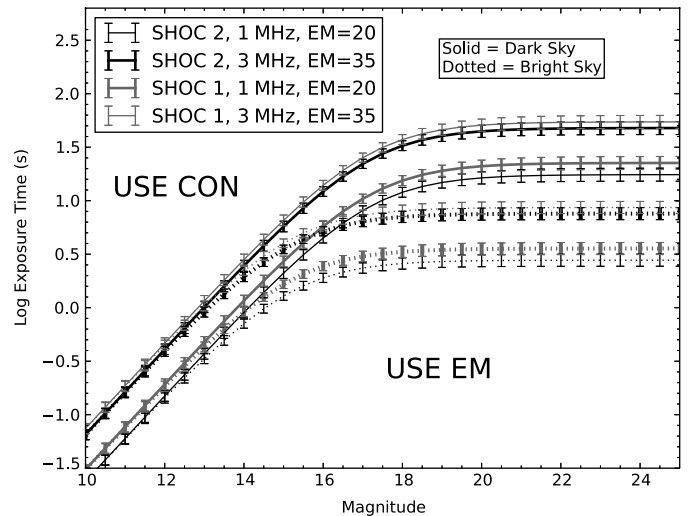[8] Available at http://shoc.saao.ac.za/Documentation.html.

FIG. 5.—Logarithm of the exposure time at which the S/N in CON and corresponding EM modes are equal. *Solid lines* indicate values for dark sky conditions (surface brightness of $21.7\ \mathrm{mag\,arcsec}^{-2}$) with *dotted lines* showing values for bright sky conditions (surface brightness of $19.7\ \mathrm{mag\,arcsec}^{-2}$). Values are for the 1.9 m without the focal reducer. Data are shown for the 1 MHz CON and EM and 3 MHz CON and EM modes in SHOC 1 and 2, including error bars. Exposure times below the lines will result in a higher S/N in the EM mode, while exposure times above result in higher S/N in the CON mode. The offsets between the values for SHOC 1 and 2, and those of the 1 and 3 MHz modes, are caused by slightly higher CON read noise values in SHOC 2 (vs. SHOC 1) and the 3 MHz mode (vs. 1 MHz).

4. DATA REDUCTION AND SCIENCE OBSERVATIONS

High-time resolution applications often benefit from near real-time data analysis. For example, the knowledge that a source is varying, or how much it is varying, can influence observations for the remainder of the night. A data-reduction pipeline was thus developed during the final stages of the commissioning phase to allow quick photometry and light curve generation at the telescope, within the operational constraints of the instrument (i.e., data cubes must be completed and copied from the control computer before data analysis can be done). This pipeline will be adjusted to accommodate user requirements that are/were not initially incorporated.

The first science demonstration of SHOC data was of a dwarf nova superoutburst of CC Sculptoris in 2011 November, presented in Woudt et al. (2012b). Three examples of SHOC being used for scientific applications are provided here: observations of predicted stellar occultations by Pluto, high-speed photometry of faint cataclysmic variable stars and flickering in a recurrent nova.

4.1. Data Reduction Pipeline

A PYTHON-based data reduction pipeline is available to users at the telescope and runs on the SAAO server. It facilitates the following major tasks: (i) item correction of the FITS
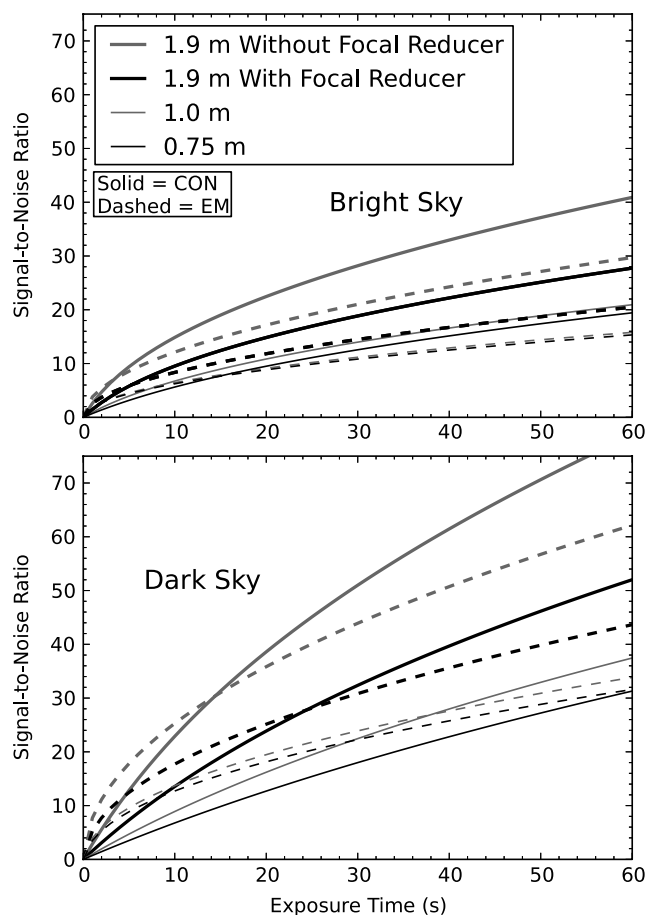
FIG. 6.—Signal-to-noise ratios calculated from eqs. (1) and (2) for a $V = 18$ mag star on the 0.75, 1.0 and 1.9 m telescopes with and without the focal reducer in SHOC 1's 1 MHz EM and CON modes. *Top*: Bright sky observing conditions, assuming sky background 19.7 mag arcsec^{-2}. *Bottom*: Dark observing conditions, assuming sky background 21.7 mag arcsec^{-2}. Assumptions were: an appropriate binning for 1.5″ seeing (1.9 m without focal reducer: 6×6; 1.9 m with focal reducer: 3×3; 1.0 m: 3×3; 0.75 m: 2×2), an EM gain of 25 and a photometry aperture of radius 9 pixels (approximately 3 times the FWHM).

headers (using PyFITS,[9] Barrett et al. 1999), (ii) running IRAF (Tody 1986) photometry tasks using PyRAF (STScI 2012), (iii) extraction of raw and differential light curves per source, and (iv) plotting of results (using GNUPLOT). The pipeline and a user manual may be downloaded following links from the SHOC website[10] or directly from its own website.[11] Users should refer to the README provided online for instructions downloading and running the scripts.

In short, the pipeline employs aperture photometry by the IRAF routines noao, digiphot and daophot (Stetson 1987), using

[9] See http://www.stsci.edu/institute/software_hardware/pyfits.
[10] See http://shoc.saao.ac.za/.
[11] See http://www.saao.ac.za/~marissa/SHOCpipeline/.

a curve of growth method to determine the optimal aperture size through the use of the photcal, mkapfile routine (Davis & Gigoux 1993). The outputs generated include (i) an ASCII-format file containing a table of instrumental magnitudes and start times for each exposure for the target and all comparison stars, (ii) a plot of the instrumental magnitudes versus time for each target and (iii) if desired, a table and plot for differential photometry between the target and user-selected comparison stars. Parameters that can easily be set by the user include (amongst others) the range of trial apertures, the threshold for selecting targets and comparison stars in the field, and the usage of flats or biases from which masters are created.

A quick-look mode is also available allowing the user to skip past the more time consuming prereductions, such as bias correction and flat fielding, and rapidly extract raw light curves to get an indication of source variability and data quality. Note that these results are not intended to be of publication quality and are strongly dependent on the parameters set by the user. Tweaking the parameters and rerunning the pipeline when time is not a critical factor may return higher quality results.

4.2. Two Stellar Appulses by Pluto

The shadow paths for two stellar occultations by Pluto were predicted to fall near Sutherland, within a few days of each other, in 2012 June.[12] The events were for two stars with Second U.S. Naval Observatory CCD Astrograph Catalog magnitudes 15.7 and 13.8 (the U.S. Naval Observatory CCD Astrograph Catalog (UCAC) bandpass lies between that of V and R), had shadow velocities of 23.13 km s^{-1} and 23.08 km s^{-1} and were predicted to occur at $23{:}10{:}44 \pm 00{:}00{:}42$ UT on 2012 June 12 and $03{:}23{:}08 \pm 00{:}00{:}42$ UT on 2012 June 14. The errors on the predicted positions for the stars and Pluto corresponded to errors in the north-south distances from the shadow centers of just under 600 km (declination error ∼0.03″ at position angle −6°; right ascension errors correspond to errors in the midtime of the event). Sutherland was predicted to be south of the shadow paths by more than six sigma and 15 sigma for the two events, respectively. Nonetheless, Pluto occultations are particularly interesting given the atmospheric changes observed in recent years (e.g., Elliot et al. 2007; Young et al. 2008; Person et al. 2013), combined with the anticipated arrival of NASA's *New Horizons* spacecraft in 2015, and are rare enough to merit the observing attempts. These events provided an excellent opportunity to carry out science commissioning of SHOC, since the primary motivation for construction of the instruments was observing stellar occultations by small bodies in the solar system.

Data were taken using the 1.9 m telescope with no filter. On June 12, SHOC was employed in full-frame, 1 MHz conventional mode with $2.4\times$ gain and 8×8 binning (corresponding

[12] See http://occult.mit.edu/research/occultationPredictionsArchive.php.

to read noise of 7.5 e^- and gain 1.7 e^- ADU^{-1}). A 14,000-frame data cube was taken starting at 22:32:00 UT with a cadence of 0.3 s. The conditions were clear with seeing ranging from 2″ to 3″. On June 14, SHOC was employed in 3 MHz conventional mode with 2.4× gain, and 5 × 5 binning (corresponding to read noise of 11.6 e^- and gain 4.2 e^- ADU^{-1}). This configuration required a slight reduction from the full frame since 1024 pixels are not evenly divisible by five. A 24,000-frame data cube was taken starting at 02:42:00 UT with a cadence of 0.2 s. Once more, conditions were clear with seeing stable at approximately 1″. Every frame in each data cube was triggered individually by the GPS, thus the uncertainty on the absolute start time of each frame was better than 10 μs.

Because stellar occultations result in the merging of the light profiles of the star and occulting body, standard pipelines used to derive light curves can be difficult to employ. However, the June 12 event had a relatively uncrowded field, and a light curve was created using the SHOC data reduction pipeline described in § 4.1. The optimal aperture size was determined to be 7 superpixels diameter (4.3″), and a comparison star of similar magnitude was used to create a differential light curve. Data taken prior to the event, when Pluto and the star were well separated, were analyzed to calculate a background fraction of 0.79. The background fraction is defined as flux$_{\text{Pluto}}$/(flux$_{\text{Pluto}}$ + flux$_{\text{star}}$), allowing the light curve to be normalized to the expected zero (occulted) and full (unocculted) flux levels. The resulting light curve, shown in Figure 7, has a spatial resolution of 6.9 km and a S/N of 40 per atmospheric scale height of 60 km on Pluto. Note that the S/N value here is that commonly used for occultations, the mean divided by the standard deviation of the baseline flux.

The June 14 field was too crowded to return proper results using the standard pipeline. Thus, we performed circular aperture photometry on each frame for Pluto combined with the target star, and a comparison star with similar magnitude. The background was the mean of a selection of the darkest regions surrounding each target. An aperture size of 8 superpixels diameter (3.04″) returned the cleanest differential light curve. The light curve was then normalized using a background fraction of 0.29, which was calculated from frames in which Pluto and the star were distinct. The normalized light curve is shown in Figure 7. Note that the analysis was fairly difficult due to the close proximity of a bright field star to Pluto—the spiky features in the light curve are not thought to be real but are most likely an artifact of the photometry. Slightly larger apertures produced light curves with higher S/Ns. However, the larger apertures showed spikes that are thought to be due to brighter pixels moving in and out of the aperture as a result of the seeing. This star was significantly brighter than that of the previous event, and the occultation S/N is 157 per Pluto scale height with a spatial resolution of 4.6 km.

The most notable characteristic of Figure 7 is actually a missing feature: the occultations. No occultation was detected on
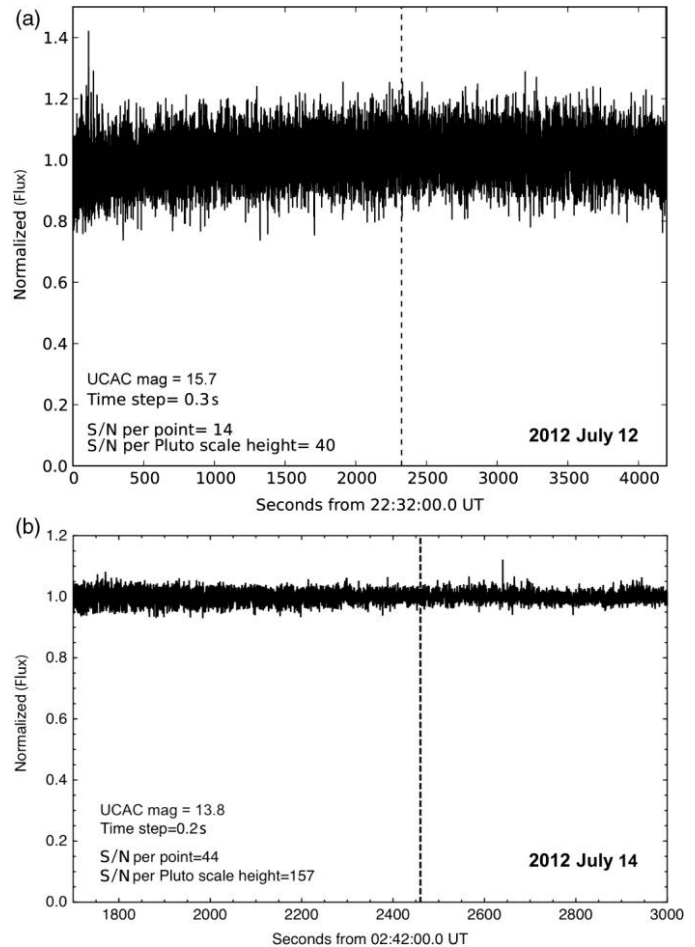

FIG. 7.—Light curves from the predicted stellar occultations by Pluto on 2012 June 12 and 14. The normalized flux of the stars is plotted vs. time, with the predicted midtimes of the events indicated by *dotted vertical lines*. Unfortunately, the shadow paths did not go over the SAAO for either of these events; however, the appulse data demonstrate the high quality that would have been obtained had an occultation been observed. The S/N per Pluto scale height is approximately 40 and 157 for the 0.3 and 0.2 s observations of stars having UCAC magnitudes 15.7 and 13.8, respectively. The spike in the bottom plot is likely not real—it is an effect of the aperture photometry method and crowded field.

either date, effectively converting these events into appulses. This result is consistent with the predictions. However, a significant amount of astrometric data, which were not obtained for these events, would be required to accurately measure the closest approaches and directions for each appulse. The appulse light curves thus serve solely to demonstrate that SHOC would have produced high quality data had occultations been observed. In fact, the quality of the appulse light curve from 2012 June 12 is comparable to data from the Pluto occultation of P571 (R magnitude = 15.8) on 2008 June 23, observed at a cadence of 0.25 s from MORIS on the 3 m Infrared Telescope Facility, which achieved S/N of 35 per Pluto scale height (Gulbis et al. 2011).

4.3. Photometric Survey of Faint Cataclysmic Variables

The University of Cape Town CCD CV survey has been observing faint cataclysmic variable stars (CVs) in the Southern Hemisphere, since 2001 (see Woudt et al. 2012a and references therein). Whereas the University of Cape Town CCD instrument (UCT CCD; O'Donoghue 1995) was used prior to 2012, SHOC is now used for all UCT CCD CV survey observations.

CVs are binary star systems in which a white dwarf primary accretes matter from a low-mass secondary companion (see Warner 1995 for a review). Typically, orbital periods of CVs are on the order of a few minutes to a few hours. As evolutionary models for these objects rely on large numbers of orbital periods (e.g., Gänsicke et al. 2009), one of the primary aims of the high-speed photometric survey is to classify newly discovered systems and determine their orbital periods. Additional aims are to investigate the short period oscillations seen in the light curves and identify targets for further follow-up studies on large telescopes such as the Southern African Large Telescope.

Figure 8 gives an example of the survey work from Coppejans et al. 2013. The light curves are of CSS110513: 210846-035031 (hereafter, CSS2108-03),[13] which was discovered in outburst by the Catalina Real-time Transient Survey (CRTS; Drake et al. 2009) on 2011 May 13.

The observations, taken in 2011 October, were performed with SHOC 1 in the 1 MHz conventional mode with $2.4\times$ gain, mounted on the 1.9 m and 1.0 m telescopes. While no filter was used in order to get the highest possible S/N, the observations were calibrated to the Sloan r photometric system using the method described in Woudt et al. (2012a). The observing log for the observations is given in Table 3.

As demonstrated in Figure 8, CVs can vary by more than a magnitude over the course of an observation. CSS2108-03 shows eclipses of delta $r \sim 1.5$ mag, which indicate that it is a high inclination system where the hot white dwarf is eclipsed by the cooler secondary star. The exposure times (listed in Table 3) were chosen such that CSS2108-03 would be detected during eclipse and the time resolution would still be sufficient to sample features with periods on the order of minutes. Using equation (1), the S/N just before the eclipse was calculated to be around 31 for the 1.9 m run (run number S8107).

Using a combination of Fourier analysis and phase folding, Coppejans et al. (2013) determined that the orbital period of this system is 0.15690[5] days and the ephemeris for mid-eclipse is given by $HJD_{ec} = 2,455,846.3725 + 0.15690[5]E$ (the uncertainty on the last digit is indicated in brackets and E is the cycle number).

From the eclipse depth it was found that the inclination of the system is larger than 70°. Eclipse deconvolution of higher time resolution observations (on a larger telescope) can now be used to refine this estimate, as well as provide parameters such as the
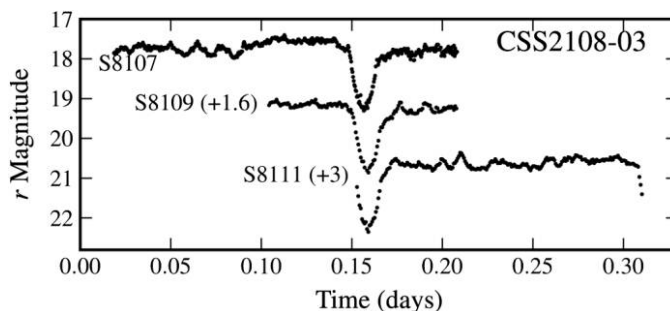

FIG. 8.—Light curves for CSS2108-03 taken with SHOC. The telescopes and exposure times for each dataset are listed in Table 3. For display purposes, the observing runs are offset vertically by the amount indicated in round brackets. The ~1.5 mag eclipses are produced by the obscuration of the hot white dwarf by the secondary star. Figure from Coppejans et al. (2013).

inclination and mass ratio. As the eclipsing systems can be used to deduce these parameters, they are important tools for evolutionary studies (e.g., Littlefair et al. 2008).

The 7 yr CRTS light curve for this object[14] shows a number of dwarf nova outbursts. These are periods of increased luminosity that are triggered by instabilities in the accretion disc (see Warner 1995). They typically range from 2 to 5 mag and recur on timescales of days to months. This behavior is characteristic of a subclass of CV known as dwarf novae.

An alternative example where SHOC was used to probe higher frequency modulations in CVs was the discovery of the intermediate polar nature of the dwarf nova CC Scl (Woudt et al. 2012b). SHOC observations were triggered following a superoutburst of CC Scl in 2011 November, reported by the CRTS, when CC Scl reached $V \sim 13.4$ mag during peak of outburst.

With SHOC mounted on the 1.0 m telescope of the SAAO during 2011 November, exposure times as short as 1 s were used to probe the fastest time scale of variability in CC Scl (to search for dwarf nova oscillations on time scales of 10–30 s, see Warner & Woudt 2002, or a rotation period of the white dwarf primary, e.g., Woudt et al. 2009).

CC Scl revealed a coherent photometric modulation at 389.49 s during its superoutburst, which is associated with the rotation period of the white dwarf primary. This interpretation was confirmed by simultaneous X-ray observations with NASA's *Swift* spacecraft, which showed a modulation on the same period, establishing the magnetic nature of the white dwarf primary (Woudt et al. 2012b).

In summary, SHOC's high-speed photometric observations of the eclipsing dwarf nova CSS2108-03 and intermediate polar CC Scl were used in order to characterize these systems and determine the periods of their photometric modulations. These

---

[13] See http://nesssi.cacr.caltech.edu/catalina/AllCV.html.

[14] CRTS transient ID: CSS110513:210846-035031.

Run No.	Date of obs. (start of night, UT)	HJD of first obs. (−2450000.0)	Length (hr)	Integration time (s)	Telescope	Sloan r (mag)[a]
S8107 …….	2011 Oct 11	5846.2343	4.5482	30	1.9 m	17.7
S8109 …….	2011 Oct 15	5850.2412	2.4834	60	1.0 m	17.6
S8111 …….	2011 Oct 16	5851.2308	3.7767	60	1.0 m	17.6

[a] Magnitudes values correspond to the mean magnitudes out of eclipse.

observations form part of an ongoing survey of faint CVs, for which SHOC will be employed from now on.

4.4. Flickering in RS Ophiuchi

Recurrent novae (RNe) are a subclass of symbiotic stars in which multiple nova outbursts have been observed. RS Ophiuchi has undergone six recorded outbursts in the last 114 years, making it the most active known symbiotic RN. Outbursts are fuelled by accretion of material from an evolved, cool giant to a hotter, more massive, compact companion and result in a rapid rise in brightness of ∼5–6 mag within a day.

In quiescence, the light curve of RS Oph varies by up to 20% in white light (Kenyon 1986). These stochastic or aperiodic brightness variations are known as flickering, with "strong" flickering considered to be more than ∼0.2 mag (e.g., Sokoloski et al. 2001). Flickering is considered indicative of accretion onto a white dwarf (e.g., Robinson 1976), and assuming the observed

FIG. 9.—The 2011 October 3 SHOC differential light curve of RS Oph (*at top; filled circles*) compared with a differential light curve obtained with the SAAO CCD (*at bottom; open circles*) on the same telescope in similarly poor sky conditions on 2006 October 21 (from Worters et al. 2007); SHOC demonstrating a significant increase in temporal resolution. The central light curve (*filled circles*) shows the SHOC data binned to the SAAO CCD time resolution, speculatively demonstrating at least comparable S/N. Light curves are normalized and shifted in magnitude for display purposes. Zero on the abscissa denotes the start time of the observation. Discontinuities in the light curves are due to cloud.

flickering originates in an accretion disc, it can be used to place constraints on the mass-transfer rate within these systems.

To this end, observations of the quiescent recurrent nova RS Oph were made on 2010 October 3 with SHOC 1 mounted on the SAAO 1.0 m telescope. The instrument was used in 1 MHz electron-multiplying mode, with an EM gain of 70 for the first cube and 75 for the following four, a pre-amp gain of 2.4× and pixel binning of 2 × 2. Observations were made using a Bessel V filter.

Five consecutive data cubes were obtained, consisting of a total of 1375 frames with 86.7 minutes total duration. Exposures were triggered internally, yielding an absolute timing accuracy of ∼1 s on the start of each cube. The integration time was 4.0 s for the first cube and 3.5 s for the subsequent four; a factor of 8 times shorter than was possible during earlier such observations with the SAAO CCD on the same telescope (Worters et al. 2007), and 4 times shorter than the minimum published cycle time for sampling V-band flickering (Zamanov et al. 2010).

Data were reduced using the SHOC pipeline extracting light curves of RS Oph and two comparison stars (lower limit of $V = 14.4$ mag) with an optimal aperture size of 15 superpixels. The resultant differential light curve is depicted in Figure 9. Flickering was detected with an amplitude of 0.025 mag. Sky conditions were suboptimal, with cirrus reducing the S/N and limiting the scope of useful analysis. The notable result is the significant gain in temporal resolution afforded by SHOC over existing instruments at the SAAO; the ability to detect variability on shorter timescales will allow improved estimates of the inner disc radius, tighter constraints to be placed on accretion rates, identification of inner disc disruption, and detection of signatures of turbulence and magnetic activity in these objects.

5. SUMMARY AND FUTURE WORK

We present SHOC, a new a high-speed, accurately-timed, optical instrument for use on the 1.9, 1.0, and 0.75 m telescopes at the SAAO site in Sutherland. Two full SHOC systems have been constructed and can be used simultaneously on different telescopes. In addition, a third system consisting of all components, excluding a camera, was built to allow for fast hardware swapping in case of a malfunction.

SHOC's main aim is to do high-speed, high-S/N, optical photometry, but it can also be used for other types of imaging.
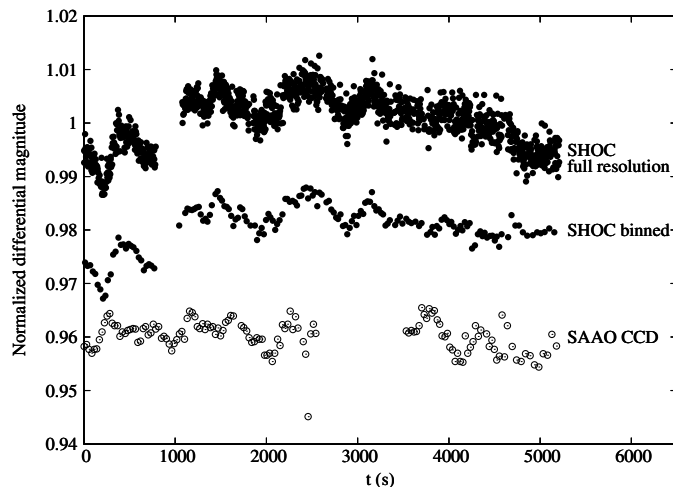
To facilitate these capabilities, SHOC has a moderate field of view, low read noise, low dark current, high quantum efficiency, microsecond single frame timing accuracy and a variety of user selectable parameters such as amplifiers, binning and subframing. In addition, the ability to select whether to use the EM or CON modes allows the highest possible S/Ns to be obtained when observing both faint and bright targets. When utilizing the EM modes, the target signal is boosted, thereby effectively reducing read noise to subelectron levels, allowing shorter exposure times to be used and fainter targets to be observed. Although no testing was done towards this, the EM modes potentially allow SHOC to be used for lucky imaging (e.g., Mackay et al. 2004; Oscoz et al. 2008).

Both SHOC systems have undergone extensive testing and characterization. Amongst other things, this included confirming that the theoretical equations provide a reasonable estimate for S/N as a function of mode, exposure time, stellar magnitude and sky brightness. These equations can thus guide observers in selecting the optimal telescope, mode, exposure time and lunar conditions for their target. Importantly, we provide a framework for comparing data quality in EM versus CON modes for standard types of observations carried out at the SAAO.

Three examples of science done with SHOC are provided here: (i) stellar occultations by small bodies in the solar system, (ii) studies of cataclysmic variable systems and (iii) flickering in a recurrent nova. While these demonstrate that the SHOC systems are currently operational and obtaining high-quality science data, there is still work remaining. The most important outstanding task is software integration. This work is required in order to combine all telescope, camera, filter, and GPS information into the data headers, as well as allow improved functionality such as scripting of filter sequences and integrating the GPS control into that of the camera. Less urgent upgrades include plans to add a shutter (the cameras do not have internal shutters) and designing and building a new focal reducer for the 1.9 m in order to increase throughput for observations requiring the largest FoV. Considering that the seeing at Sutherland seldom drops below 0.8″, it is clear from Table 2 that SHOC's plate scale can be significantly increased, up to around 0.3 arcsec/pixel, without undersampling the point-spread function. This will not only increase SHOC's ability for doing imaging but also increase the maximum separation between a target and comparison star when doing differential photometry.

The SAAO telescopes are a national facility and applications are accepted from astronomers around the world. For more details on SHOC, including a user manual and how to apply for time, please see http://shoc.saao.ac.za and http://www.saao.ac.za.

REFERENCES

Barrett, P. E., & Bridgman, W. T. 1999, in Astronomical Data Analysis Software and Systems VIII, Astronomical Society of the Pacific Conference Series, 172, 483, http://adsabs.harvard.edu/abs/1999ASPC..172..483B

Basden, A. G., & Haniff, C. A. 2004, MNRAS, 347, 1187

Buckley, D.A.H., et al. 2010, Proc. SPIE, 7735, 773559

Coppejans, R. 2013, M.Sc. thesis, University of Cape Town

Coppejans, D. L., et al. 2013, MNRAS, submitted

Daigle, O., Carignan, C., Gach, J.-L., Guillaume, C., Lessaed, S., Fortin, C.-A., & Blais-Ouellette, S. 2009, PASP, 121, 866

Davis, L. E., & Gigoux, P. 1993, in ASP Conf. Ser. 52, Astronomical Data Analysis Software and Systems II, ed. R. J. Hanisch, R. J. Brissenden, & J. Barnes (San Francisco: ASP), 479

Drake, A. J., et al. 2009, ApJ, 696, 870

Elliot, J. L., et al. 2007, AJ, 134, 1

———. 2010, Nature, 465, 897

Gach, J. L., Balard, P., Daigle, O., Destefanis, G., Feautrier, P., Guillaume, C., & Rothman, J. 2009, EAS Publications Series, 37, 255

Gänsicke, B. T., et al. 2009, MNRAS, 397, 2170

Gulbis, A. A. S., et al. 2006, Nature, 439, 48

———. 2011, PASP, 123, 461

Honeycutt, R. K. 1992, PASP, 104, 435

Hynecek, J. 2001, IEEE Trans. Electron Dev., 48, 2238

Janesick, J. R. 2001, Scientific Charge-Coupled Devices (Bellingham: SPIE Optical Engineering Press)

Jerram, P., et al. 2001, Proc. SPIE, 4306, 178

Kenyon, S. J. 1986, Symbiotic Stars (Cambridge: Cambridge University Press)

Krisciunas, K., & Schaefer, B. E. 1991, PASP, 103, 1033

Landolt, A. U. 1992, AJ, 104, 340

Littlefair, S. P., Dhillon, V. S., Marsh, T. R., Gänsicke, B. T., Southworth, J., Baraffe, I., Watson, C. A., & Copperwheat, C. 2008, MNRAS, 388, 1582

Mackay, C. D., Baldwin, J., Law, N., & Warner, P. 2004, Proc. SPIE, 5492, 128

Merline, W. J., & Howell, S. B. 1995, Exp. Astron., 6, 163

O'Donoghue, D. 1995, Baltic Astron., 4, 519

O'Donoghue, D., et al. 2006, MNRAS, 372, 151

Oscoz, A., et al. 2008, Proc. SPIE, 7014, 10

Pepper, J., Kuhn, R. B., Siverd, R., James, D., & Stassun, K. 2012, PASP, 124, 230

Person, M. J., et al. 2013, AJ, submitted

Potter, S. B., et al. 2011, MNRAS, 416, 2202

Robinson, E. L. 1976, ARA&A, 14, 119

Sokoloski, J. L., Bildsten, L., & Ho, W. C. G. 2001, MNRAS, 326, 553

Souza, S. P., Babcock, B. A., Pasachoff, J. M., Gulbis, A. A. S., Elliot, J. L., Person, M. J., & Gangestad, J. W. 2006, PASP, 118, 1550

Stetson, P. B. 1987, PASP, 99, 191

STScI. 2012, in Astrophysics Source Code Library, Astronomy Picture of the Day, record ascl: 1207.011, http://ascl.net/1207.011

Tody, D. 1986, Proc. SPIE, 627, 733

Warner, B. 1995, Cataclysmic Variable Stars (Cambridge: Cambridge University Press)

Warner, B., & Woudt, P. A. 2002, MNRAS, 335, 84

Worters, H. L., Eyres, S. P. S., Bromage, G. E., & Osborne, J. P. 2007, MNRAS, 379, 1557

Woudt, P. A., Warner, B., Osborne, J., & Page, K. 2009, MNRAS, 395, 2177

Woudt, P. A., Warner, B., O'Donoghue, D., Buckley, D. A. H., Still, M., Romero-Colmenero, E., & Vaisanen, P. 2010, MNRAS, 401, 500

Woudt, P. A., Warner, B., de Bude, D., Macfarlane, S., Schurch, M. P. E., & Zietsman, E. 2012a, MNRAS, 421, 2414

Woudt, P. A., et al. 2012b, MNRAS, 427, 1004

Young, E. F., et al. 2008, AJ, 136, 1757

Zamanov, R., et al. 2010, MNRAS, 404, 381